Modeling primary microcephaly with human brain organoids reveals fundamental roles of CIT kinase activity

Modeling primary microcephaly with human brain organoids reveals fundamental roles of CIT kinase activity

Gianmarco Pallavicini* [1,2], Amanda Moccia* [3], Giorgia Iegiani* [1,2], Roberta Parolisi[1,2], Emily R. Peirent [4], Gaia Elena Berto[1,2], Martina Lorenzati[1,2], Rami Y. Tshuva[5], Alessia Ferraro [1,2], Fiorella Balzac[6], Emilia Turco[5], Shachi Salvi[3], Hedvig F. Myklebust[3], Sophia Wang[3], Julia Eisenberg[3,7], Maushmi Chitale[3], Navjit Girgla[3], Enrica Boda[1,2], Orly Reiner [5], Annalisa Buffo[1,2], Ferdinando Di Cunto[$1,2] and Stephanie L. Bielas[$3,4,7]

1. Neuroscience Institute Cavalieri Ottolenghi, Turin, Italy.

2. Department of Neuroscience 'Rita Levi Montalcini', University of Turin, Italy

3. Department of Human Genetics, University of Michigan Medical School, Ann Arbor, MI, USA

4. Neuroscience Graduate Program, University of Michigan Medical School, Ann Arbor, MI, USA

5. Departments of Molecular Genetics and Molecular Neuroscience, Weizmann Institute of Science, Rehovot, Israel

6. Department of Molecular Biotechnology and Health Sciences, University of Turin, Italy

7.Department of Pediatrics, University of Michigan Medical School, Ann Arbor, MI, USA

* These authors contributed equally to this work

$ Corresponding author:

Ferdinando Di Cunto (Ferdinando Di Cunto, Neuroscience Institute Cavalieri Ottolenghi Regione Gonzole, 10, 10043 Orbassano (TO), Italy,+39-011-6706616, ferdinando.dicunto@unito.it)

Stephanie L. Bielas (Stephanie L. Bielas, Department of Human Genetics, University of Michigan Medical School, 3703 Med Sci II, 1241 E. Catherine St., Ann Arbor, Michigan, 48109-5618, USA, 1-734-647-8890, sbielas@med.umich.edu)

The authors have declared that no conflict of interest exists.

Abstract

Brain size and cellular heterogeneity are tightly regulated by species-specific proliferation and differentiation of multipotent neural progenitor cells (NPCs). Errors in this process are among the mechanisms of primary hereditary microcephaly (MCPH), a group of disorders characterized by reduced brain size and intellectual disability. Biallelic *CIT* missense variants that disrupt kinase function ($CIT^{KI/KI}$) and frameshift loss-of-function variants ($CIT^{FS/FS}$) are the genetic basis for MCPH17; however, the function of CIT catalytic activity in brain development and NPC cytokinesis is unknown. Therefore, we created the $Cit^{KI/KI}$ mouse model and found that it does not phenocopy human microcephaly, unlike biallelic $Cit^{FS/FS}$ animals. Nevertheless, both *Cit* models exhibited binucleation, DNA damage, and apoptosis. To investigate human-specific mechanisms of *CIT* microcephaly, we generated $CIT^{KI/KI}$ and $CIT^{FS/FS}$ human forebrain organoids. We found that $CIT^{KI/KI}$ and $CIT^{FS/FS}$ organoids lose cytoarchitectural complexity, transitioning from pseudostratified to simple neuroepithelium. This change was associated with defects that disrupt polarity of NPC cytokinesis, in addition to elevating apoptosis. Together, our results indicate that both CIT catalytic and scaffolding functions in NPC cytokinesis are critical for human corticogenesis. Species differences in corticogenesis and the dynamic 3D features of NPC mitosis underscore the utility of human forebrain organoid models for understanding human microcephaly.

Introduction

The mammalian cerebral cortex forms through a species-specific sequence of neural precursor cell proliferation and differentiation events (1, 2). Neuro-epithelial stem cells expand through a series of symmetric proliferative divisions and then give rise to multipotent apical neural radial glia progenitor cells (aNPCs). In the ventricular zone, aNPCs divide symmetrically to produce additional multipotent progenitors and asymmetrically to produce basal neural radial glia progenitor cells (bNPCs) and intermediate progenitor cells (IPCs), which continue to proliferate in the outer-subventricular zone or terminally differentiate to excitatory neuron subtypes (3). Expansion of multipotent aNPCs by symmetric proliferation and generation of progeny through asymmetric cell division are carefully regulated species-specific features of corticogenesis that contribute to the final size and folding of the cerebral cortex (1, 2, 4). Given the consequential role of aNPC symmetrical division on brain size, the apical-basal polarity of aNPCs is tightly controlled. aNPCs span the breadth of neuroepithelium with apical end-feet secured at the ventricular border by adhesion junctions that contain overlapping fate and polarity factors. Precise distribution of fate determinants between aNPC daughter progeny determines cell fate. During neurogenesis, cleavage furrow constriction of mitotic aNPCs in neuroepithelium is polarized; contractile ring constriction occurs from the basal to apical membrane to localize abscission at the apical border of the cell, adjacent to the ventricle (4). The position of the mitotic spindle relative to the apical border of aNPCs, shifting between perpendicular to oblique or even parallel, is also critical in the transition from symmetric to asymmetric divisions (5). The importance of this biology for corticogenesis is accentuated by primary hereditary microcephaly (MCPH) and microlissencephaly that result from errors in this developmental process (6, 7).

MCPH-associated proteins participate in many biological processes that impact aNPC proliferation and differentiation (7–11). Disentangling the complex physiological relationships between MCPH genes is complicated by the limited knowledge about their functional interactions and the difficulty of modeling human microcephaly in rodents, which do not recapitulate all details of human cortical development. Indeed, inactivation of MCPH genes in mice frequently produces significantly milder phenotypes than those observed in affected individuals (12, 13). We previously identified pathogenic biallelic variants in *CIT* (OMIM ID: 605629) as the genetic basis for MCPH17 (14, 15). *CIT* represents a growing list of human genetic findings linking defects in cytokinesis machinery to clinical features of severe microcephaly. An overarching feature of these findings is their disproportionate impact on brain development despite widespread expression across tissues, highlighting a unique vulnerability of the brain to cytokinesis defects. *CIT* encodes a ser/thr protein kinase (CIT-K) that localizes to the contractile ring and midbody during cytokinesis. CIT-K is functionally critical for cytokinesis completion, midbody positioning, abscission, and maintenance of genomic integrity (16–20). CIT-K is characterized by an N-terminal kinase domain and C-terminal protein interaction domains. The C-terminal domains permit integration into the contractile ring and midbody, which is required for scaffolding functions. Biallelic *CIT* missense variants that disrupt kinase function (KI) and loss-of-function (LOF) frameshift (FS) variants that destroy both kinase and scaffolding functions are the genetic basis of microcephaly and microlissencephaly, respectively (14, 15, 21, 22). The increasing severity of these clinical phenotypes indicate that both kinase and scaffolding functions are crucial for brain development.

In this report, we describe complementary mouse and human *CIT* kinase-inactive models generated to discriminate the developmental mechanisms of CIT-K kinase function from the more severe *CIT* LOF corticogenesis phenotypes. *Cit* LOF rodent models display severe microcephaly as result of altered neurogenesis, binucleation, and TP53-dependent apoptosis (18, 23, 24). $Cit^{KI/KI}$ mice do not phenocopy MCPH17 microcephaly, although they display aNPC molecular phenotypes consistent with *Cit* LOF models. Similar to the described mouse models, progressively more severe molecular pathology was observed between $CIT^{KI/KI}$ and $CIT^{FS/FS}$ human 3D forebrain organoids. However, both genotypes display striking alterations in the polarized organization and structural integrity of neural rosette neuroepithelium, revealing a function of CIT-K kinase activity in aNPC cytokinesis that is critical for early brain development. Our results underscore the relevance of species-specific sensitivity to CIT-K cytokinesis functions and further highlight human 3D forebrain organoids as a fundamental model for better understanding human microcephaly.

Results

Brain size is unchanged in *Cit-K* kinase-inactive mouse model

To investigate the role of CIT-K catalytic activity in brain development, a new mutant mouse model was generated. Two-nucleotides were edited using traditional mouse embryonic stem cell-based knock-in technologies (25) to generate a *Cit* (c.376_377AA>GC; p.K126A) kinase inactive (KI) mouse line. This *Cit* missense substitution is similar to *CIT* missense variants described in individuals with MCPH17 microcephaly (Figure S1, A-E)(15). The K126A amino acid substitution was previously shown to fully abolish CIT-K kinase activity (Figure S1B)(26). Homozygous $Cit^{KI/KI}$ pups were born at expected Mendelian ratios. CIT-K has highest expression in multipotent progenitors. Western blot analysis of postnatal day (P) 4 cerebellum and cortex showed a 40% reduction in CIT-K expression in the cerebellum of $Cit^{KI/KI}$ mice and normal expression of CIT-N, a shorter brain-specific isoform lacking the amino terminal kinase domain (Figure S1, F-G) (27, 28). We did not detect CIT-K expression in the cortex at this developmental timepoint (Figure S1, F-I), consistent with limited aNPC proliferation postnatally (27–29). Since a 50% reduction of wild-type CIT-K has not been associated with a measurable phenotype (18, 23), comparing $Cit^{KI/KI}$ animals to homozygous frameshift ($Cit^{FS/FS}$) and wild-type control mice will allow the phenotypic contribution of catalytic versus scaffolding activities of CIT-K to be assessed. Unlike $Cit^{FS/FS}$ mice, $Cit^{KI/KI}$ pups were indistinguishable from control littermates based on head morphology upon physical exam and were not microcephalic (Figure 1A and S2A). $Cit^{KI/KI}$ mice exhibited normal growth rate and were inter-fertile. Perinatal lethality was not detected among $Cit^{KI/KI}$ pups, unlike $Cit^{FS/FS}$ mice, which die within one month of birth (Figure 1B). No significant alterations in cortical thickness, hippocampal structure, or cerebellar organization were detected

in *Cit*$^{KI/KI}$ brains (Figure 1,C-D and S2B-E). The cerebellar cortex was the most affected brain region in *Cit*$^{FS/FS}$ mice (23), with a dramatic reduction of the granule cell layer, resulting in overall hypoplasia and increased linear density of Purkinje cells (Figure 1, D-F). While the absolute number of Purkinje cells was not reduced in *Cit*$^{FS/FS}$ cerebellum, they did display altered morphology, with immature dendritic arborizations. In contrast, *Cit*$^{KI/KI}$ cerebella were not morphologically distinguishable from controls throughout postnatal development (Figure 1, C-F and S2F-H). Likewise, *Cit*$^{KI/KI}$ mice did not exhibit seizure activity or the dramatic reeling phenotype that characterizes *Cit*$^{FS/FS}$ pathology (23). Behavioral characterization of wild-type and *Cit*$^{KI/KI}$ young mice at P8.5 did not show any differences in the maturation of ambulation, ataxic phenotype (i.e. spontaneous flipping on the back) and surface righting reflex, which are evident in *Cit*$^{FS/FS}$ mice (Figure S2, I-K). Conversely, *Cit*$^{KI/KI}$ mice exhibit poor performance on the negative geotaxis test of motor coordination compared to wild-type mice (Figure S2L). This phenotype is still evident at two months of age, when assessed with the beam walking test, consistent with a persistent motor defect (Figure 1G-H and supplementary videos S1 and S2). Overall, *Cit*$^{KI/KI}$ mice are normocephalic, which contrasts with the human microcephaly associated with similar biallelic missense variants. These data indicate that the hypomorphic *Cit*-KI allele preserves many essential CIT-K functions performed during brain development. Moreover, they indicate a differential requirement of kinase activity in human and mouse corticogenesis.

Cellular phenotypes of apoptosis, DNA damage, and incomplete cytokinesis evident in Cit-K kinase-inactive brain

Cit$^{FS/FS}$ neurons are characterized by binucleation, accumulation of DNA damage, and increased apoptosis, cellular phenotypes associated with cytokinesis failure (18,

23, 30). Previous studies have identified a prominent role of TP53-dependent apoptosis in the pathogenesis of microcephaly in this model (18). We therefore characterized these cellular phenotypes in the *Cit*$^{KI/KI}$ postnatal brain. Evaluation of *Cit*$^{KI/KI}$ P4 developing cerebellum revealed a slight increase of apoptotic cells, enriched in the inner portion of the external granule cell layer, as quantified by cleaved Caspase 3 (cCASP3) immunofluorescence (Figure 2, A and B). This correlated with a significant increase in γH2AX staining in cerebellar cells, consistent with elevated DNA damage (Figure 2, C and D). While the frequencies of both apoptotic and γH2AX cells were increased in *Cit*$^{KI/KI}$ cerebellum relative to controls, the detected increases were higher in *Cit*$^{FS/FS}$ tissue. The increase of cCASP3 and γH2AX was confirmed by Western blot, where the highest level was again observed in *Cit*$^{FS/FS}$ samples (Figure 2, E-F). These *Cit*$^{KI/KI}$ phenotypes were still detected at P10, though apoptosis was not as severe as at earlier timepoints (Figure S3, A-D), suggesting *Cit*$^{KI/KI}$ pathology is not sufficient to generate cerebellar hypoplasia, but implicates a developmental mechanism that correlates with the *Cit*$^{KI/KI}$ motor coordination deficits.

A modest increase in apoptosis and DNA double strand breaks were also detected in the developing *Cit*$^{KI/KI}$ neocortex (Figure 2, G-H). This correlated with increased 53BP1 foci per NPC nucleus, an established marker of DNA double strand breaks (Figure 2, I-J). Again, phenotypes in *Cit*$^{KI/KI}$ samples were intermediate between *Cit*$^{FS/FS}$ and control values. To estimate the *Cit* genotype-dependent impact on cytokinesis completion, we measured the ratio of binucleated neurons in Nissl-stained cortical tissue at the end of cortical development (P10). *Cit*$^{KI/KI}$ mice exhibited a significant increase in binucleation much closer to the levels detected in *Cit*$^{FS/FS}$

mice, unlike other phenotypes assessed (Figure 2, K-L). We detected binucleated BLBP-positive astrocytes and SOX10-positive oligodendroglial cells scattered throughout the cortex in *Cit*$^{KI/KI}$ mice at P10, which were observed at higher frequency in *Cit*$^{FS/FS}$ mice (Figure S3, E-F), as previously demonstrated (30). These results indicate that CIT kinase activity is required for completion of NPC cytokinesis, and incomplete cytokinesis correlates with a disproportional increase in binucleation in *Cit*$^{KI/KI}$ cortical tissue. However, the lower levels of DNA damage and apoptosis in *Cit*$^{KI/KI}$ tissue is not sufficient to produce the TP53-dependent severe microcephaly that characterizes *Cit*$^{FS/FS}$ mice.

Human model of cortical development exhibits pathogenic mechanisms of *CIT* variants

The surprising finding that hypomorphic *Cit* missense variants that disrupt kinase activity were insufficient to produce microcephaly in mice led us to investigate how altered CIT-K catalytic and scaffolding functions contribute to microcephaly and microlissencephaly in humans. Towards this aim, human in vitro models of dorsal forebrain development were generated. Induced pluripotent stem cells (iPSCs) lines from unaffected individuals (male and female *CIT*$^{+/+}$), a related control (male *CIT*$^{+/G106V}$), and affected individuals with *CIT* biallelic missense variants (female *CIT*$^{G106V/G106V}$ and male *CIT*$^{G106V/G106V}$) were reprogrammed from primary fibroblasts (Figure 3A). iPSC lines from another affected male with MCPH17 (*CIT*$^{D230V/D230V}$) allowed variability in the allelic series to be assessed. To model CIT LOF, a clinically relevant homozygous (NM_007174.3: c.312_318del; p.C105Tfs*8) frameshift deletion was introduced in exon 4 of *CIT* by CRISPR-Cas9 genome editing of the female H9 human embryonic stem cell (hESC) line to generate *CIT*$^{FS/FS}$ (Figure 3B). The *CIT*$^{KI/KI}$ iPSC lines and edited *CIT*$^{FS/FS}$ H9 lines were evaluated relative to *CIT*$^{+/KI}$

related-iPSC lines and a *CIT*$^{+/+}$ isogenic control line, respectively. The human pluripotent stem cell (hPSC) lines were analyzed by chromosomal microarray to rule out pathogenic copy number alterations (data not shown). hPSCs were differentiated to NPCs and dorsal forebrain organoids according to a dual-SMAD inhibition protocol (31). Neural rosettes in forebrain organoids recapitulate the evolutionarily conserved in vivo polarity of mammalian neuroepithelium and display polarized aNPC cytokinesis (32). The absence of the CIT-K isoform in the *CIT*$^{FS/FS}$ NPCs was confirmed by Western blotting (Figure 3C), and CIT-N is not expressed in this developmental cell type. As in the *Cit*$^{KI/KI}$ mouse model, variable reduction of CIT-K protein abundance was observed in *CIT*$^{KI/KI}$ NPCs by Western blot (Figure 3D). In organoids at 35 days of differentiation (35DD), the midbody forms at the apical border of aNPCs adjacent to the central lumen of neural rosettes (Figure 3E). This is comparable to polarized midbody placement adjacent to the lateral ventricle during in vivo corticogenesis (33). In control cells, CIT-K localizes to the midbody central bulge, the structure formed between two dividing cells at the last stage of cytokinesis, and is flanked by Aurora B (Figure 3E). CIT-K harboring missense substitutions also correctly localized to the midbody central bulge in *CIT*$^{KI/KI}$ 35DD forebrain organoids (Figure 3E). In contrast, CIT-K is absent from the midbody central bulge in *CIT*$^{FS/FS}$ 35DD organoids. Counterstaining with mitotic kinesin-like protein MKLP1 highlighted the central bulge and confirmed gross midbody structure is preserved in the absence of CIT-K expression (Figure 3F).

CIT$^{KI/KI}$ and *CIT*$^{FS/FS}$ organoids exhibit defects in pseudostratified neuroepithelium complexity

To investigate *CIT* neuropathology in developing forebrain organoids, an allelic series of *CIT* hPSC lines stably expressing fluorescent markers to label nuclei (H2B-

mCherry) and actin (Lifeact-GFP) were created using the PiggyBac transposase method (34). Labeled hPSCs were dissociated into single cell suspensions at 0 differentiation day (DD) to generate aggregates for dorsal forebrain organoid neural differentiation (Figure 4A). Aggregates were enclosed in a microfabricated compartment of fixed height between a polycarbonate membrane and glass coverslip at 7DD using an established protocol (35). The polycarbonate membrane facilitated medium exchange and gas diffusion, while the glass coverslip permitted inverted optical imaging. The compartments were filled with Matrigel hydrogel on 9DD to mimic an in vivo environment and stabilize organoid positioning. Confocal microscopy of live organoids in culture was performed at 21DD, 28DD, and 35DD to investigate the effects of biallelic *CIT KI* and *FS* variants on organoid development. Reimaging of the same neural rosettes at progressively later days of neural differentiation in culture was critical for revealing $CIT^{KI/KI}$ and $CIT^{FS/FS}$ defects. All hPSCs carrying biallelic *CIT* missense variants (female $CIT^{G106V/G106V}$, male $CIT^{G106V/G106V}$ and male $CIT^{D230V/D230V}$) were labeled and differentiated into forebrain organoids. Data for these genotypes were pooled for analysis and are shown as $CIT^{KI/KI}$. Immunofluorescent assessment of SOX2, DCX and BCL11B labeled cells in $CIT^{+/+}$, $CIT^{+/KI}$, $CIT^{KI/KI}$ and $CIT^{FS/FS}$ 35DD fixed organoids revealed tissue differentiating along a dorsal forebrain fate (Figure S4, A and B). Consistent with *CIT* pathology and in line with previous publications, we detected binucleated BCL11B cells in $CIT^{KI/KI}$ and $CIT^{FS/FS}$ organoids (Figure S4, C and D) indicating that *CIT* variants do not preclude differentiation of mature cortical neuron subtypes.

Cytoarchitecture of 21DD organoids consisted of neural rosettes composed of aNPCs extending from the apical (inner) border of a central lumen to a basal (outer)

border. Interphase aNPC nuclei are densely packed creating a pseudostratified neuroepithelium. *CIT*$^{KI/KI}$ and *CIT*$^{FS/FS}$ neural rosette cytoarchitecture is comparable to controls at 21DD, though a small dilation of the central lumen is detectable (Figure S4, E-F and Figure 4, B and C). Striking changes in the neuroepithelium organization of the same neural rosettes were observed for *CIT*-affected genotypes reimaged at 28DD and 35DD (Figure 4, B and C). While control heterozygous *CIT*$^{+/KI}$ and *CIT*$^{+/+}$ rosettes maintained pseudostratification at 28DD and 35DD, multiple *CIT*$^{KI/KI}$ and *CIT*$^{FS/FS}$ neural rosettes transitioned from pseudostratified tissue to a simple epithelial cytoarchitecture with less cellular complexity.

Reduced *CIT*$^{KI/KI}$ and *CIT*$^{FS/FS}$ tissue complexity is directly correlated to increased diameter of the neural rosette and the central lumen. We developed the rosette index (R_i) to assess this phenotype. Rosette index ($R_i=d_r/d_l$) is a ratio of neural rosette outer diameter (d_r) relative to the inner lumen diameter (d_l), which is proportional to the complexity of neural rosette pseudostratification (Figure 4D). The R_i of *CIT*$^{+/KI}$ (R_i = 6.49) and *CIT*$^{+/+}$ (R_i = 6.89) control organoids was comparable at 21DD and remained relatively stable between 21DD-35DD (Figure 4E-F). In contrast, *CIT*$^{KI/KI}$ and *CIT*$^{FS/FS}$ neural rosettes exhibited a significantly lower R_i relative to their respective controls at 21DD and continued to decrease when measured again at 28DD with *CIT*$^{KI/KI}$ at R_i = 2.29 and *CIT*$^{FS/FS}$ at R_i = 3.29. Between 28DD and 35DD, the R_i of *CIT*$^{FS/FS}$ rosettes continued to decline (R_i =2.09), while the R_i of *CIT*$^{KI/KI}$ organoids plateau, despite remaining significantly lower than the *CIT*$^{+/KI}$ control R_i (Figure 4, E-F). While the absolute *CIT*$^{KI/KI}$ and *CIT*$^{FS/FS}$ R_i values do not scale exactly with severity in affected individuals, the phenotypic trend in both allelic series is comparable and the difference is highly significant, demonstrating the reproducibility of this phenotype. Of note, cells in these structures were clearly

multinucleated with pyknotic nuclei, implicating cytokinesis defects and apoptosis in the pathogenesis of this phenotype (Figure 4, G-H). Comparable cytoarchitectural defects observed in *CIT*$^{KI/KI}$ and *CIT*$^{FS/FS}$ neural rosettes indicates that CIT-K kinase activity is critical for early human corticogenesis.

CIT-K critical for cytokinesis in 3D tissue

Growing evidence indicates that disruption of polarized cytokinesis in 3D epithelial tissue can disrupt the coordination of abscission and formation of adhesion junctions between daughter and neighboring cells (36, 37). Likewise, incomplete cytokinesis would fail to divide the apical membrane that attaches aNPCs to the central lumen of neural rosettes. These features were evaluated to determine their contribution to cytoarchitectural changes observed in *CIT*-affected organoids. Confocal imaging of rosette lumens in Lifeact-GFP-labeled 35DD organoids allowed the surface area of the aNPC apical attachments, also described as apical endfeet, to be quantified (Figure S5A). The GFP outline of apical endfeet were manually traced and the surface area was quantified (Figure S5A). The average area of *CIT*$^{+/KI}$ apical endfeet at 35DD was 5.9μm^2, while *CIT*$^{KI/KI}$ apical endfeet area was significantly increased to 12.5μm^2 (Figure 5A). An increase was also observed for the apical tiles of *CIT*$^{FS/FS}$ endfeet that measured 11.9μm^2, compared to control *CIT*$^{+/+}$ tiles that averaged 3.4μm^2 (Figure 5B). Similar results were obtained by immunofluorescence of fixed 35DD organoids, where N-Cadherin (CDH2) was used to determine the outline of apical endfeet area (Figure S5, B-D).

CIT-K is an attractive candidate to coordinate apical placement of aNPC abscission. Failure to coordinate polarized cytokinesis with adhesion junction formation can result in loss of apical attachments and delamination, a potential mechanism that

may contribute to the increased size of aNPC apical endfeet and changes to tissue complexity. Cell division placement was assessed in live-cell imaging data and with immunohistochemistry of fixed organoid tissue. According to both analyses, a high percentage of aNPC cell divisions were misplaced relative to the central lumen in *CIT*$^{KI/KI}$ organoids; ~17% of mitotic cells were not located at central lumen as is expected during normal aNPC symmetrical expansion (Figure 5, C and D) (38). This finding was corroborated by immunostaining of midbody and apical localized markers in fixed 35DD organoids (Figure S6, A and B). An increased percentage of misplaced Aurora B-marked midbodies, displaced relative to the N-cadherin apical surface marked central lumen, was quantified in *CIT*$^{KI/KI}$ compared to control organoid tissue (Figure S6, A and B). An increase of misplaced mitotically active aNPCs was also present in *CIT*$^{FS/FS}$ organoids, as shown by live-imaging (Figure 5, G-H) and analysis of midbody position with Aurora B staining of fixed organoid tissue (Figure S6, C and D). Increased apical endfeet surface area and frequency of ab-luminal midbody placement in *CIT*$^{KI/KI}$ and *CIT*$^{FS/FS}$ neural rosettes correlates with the simplification of cytoarchitecture in the corresponding organoids and highlights pathogenic mechanisms that implicates a vulnerability of the developing brain to aNPC cytokinesis defects. Additional analysis is required to determine if this phenotype correlates to the enlarged ventricles revealed by histological evaluation of *CIT*$^{FS/FS}$ post-mortem brain tissue (14).

CIT$^{KI/KI}$ and _CIT_$^{FS/FS}$ organoids exhibit mitotic defects with genotype-dependent severity

Cytokinesis delay and increased cell binucleation due to cytokinesis failure are conserved cell autonomous pathology observed in *Cit*-knockout rodent models and 2D NPCs derived from *CIT*-affected hPSC lines (14, 23, 39). To evaluate this

dynamic and transient cell biology in 3D aNPC mitosis, two-channel live-cell time-lapse imaging of H2B-mCherry/Lifeact-GFP labeled 35DD organoids was performed at 5-10 minute intervals over 8-16 hours (Figure 5C and 5G). A significantly higher frequency of profound mitotic defects, such as aNPCs mitotic failure (stalled cells that do not complete division after prometaphase), cytokinesis failure (cells with two decondensed nuclei ascending in a single Lifeact-GFP encircled NPC soma post-furrowing) and altered cleavage plane angle (Figure S6, E-H) are observed in both $CIT^{KI/KI}$ and $CIT^{FS/FS}$ organoids (Supp. videos S3-S6). Specifically, mitotic failure occurred in 18% of $CIT^{+/KI}$ NPCs and doubled to 36% in $CIT^{KI/KI}$ NPCs (Figure 5E). Likewise, mitotic failure occurred in 23% of $CIT^{+/+}$ NPCs and 44% in $CIT^{FS/FS}$ NPCs (Figure 5I). An increase in failed cytokinesis was detected in both affected genotypes (Figure 5, E and I). Frequent binucleated cells observed undergoing multipolar mitosis is further evidence of this cellular pathology. Conversely, *CIT*-genotype had a mild impact on the timing of aNPC mitosis for aNPCs that complete mitosis and continue their interkinetic nuclear migration. $CIT^{KI/KI}$ organoids did not exhibit a significant increase in aNPC mitotic duration. However, a significant delay was observed in aNPC progression from anaphase to nuclei ascension in $CIT^{KI/KI}$ organoids. On average, $CIT^{KI/KI}$ aNPCs took ~50 minutes compared to the ~30 minutes of $CIT^{+/KI}$ control aNPCs (Figure 5F). In $CIT^{FS/FS}$ organoids, the delay in aNPC progression from anaphase to nuclei ascension increased to ~52 minutes compared to the ~36 minutes of $CIT^{+/+}$ control aNPCs (Figure 5J). Together, these data demonstrate that CIT-K kinase activity is necessary for mitotic progression and timely abscission in aNPCs.

Increased DNA damage and apoptosis are conserved *CIT* neuropathology

DNA damage and apoptosis are cellular pathology that can have measurable negative impacts on aNPC proliferation, R_i, and cellularity required for pseudostratification. These features were analyzed by immunofluorescence of fixed organoid tissue differentiated from fluorescent reporter free hPSC lines. KI67, a marker of proliferation, showed a significant reduction in the percentage of KI67-positive cells per neural rosette in 35DD *CIT*$^{KI/KI}$ and *CIT*$^{FS/FS}$ organoids (Figure 6, A and B). Unlike other cellular phenotypes, this reduction was higher in *CIT* $^{KI/KI}$ organoids than *CIT*$^{FS/FS}$ organoids. DNA damage and apoptosis are established mechanisms for reducing proliferating cells from the neural progenitor pool and were evaluated to better understand the KI67 reduction across genotypes. A robust increase in γH2AX foci in KI67-positive *CIT*$^{KI/KI}$ and *CIT*$^{FS/FS}$ NPCs revealed an accumulation of DNA damage in affected tissue (Figure 6C). This is consistent with previous work showing that *CIT* LOF variants generate DNA damage accumulation in developing mouse brains and post-mortem tissue of an affected individual (23, 30, 40) and adds that loss of CIT-K kinase function is sufficient to generate DNA damage. Induction of apoptosis was associated with incomplete cytokinesis in mice (23), human brain tumor lines (40, 41), in vitro NPCs (15), and affected individuals (14). Proliferating KI67-positive cells in both *CIT*$^{KI/KI}$ and *CIT*$^{FS/FS}$ organoids exhibited a significant increase of cells co-labeled with either cCASP3 or TUNEL relative to controls (Figure 6, D-F). Of note, TUNEL positive cells were more pronounced in the *CIT*$^{KI/KI}$ KI67 progenitors, while cCASP3 positive cells were more pronounced in *CIT*$^{FS/FS}$ tissue (Figure 6, D-F). In this comparison, the TUNEL assay may detect DNA damage and underestimate apoptosis (42). Taken together, these results suggest that damaged DNA may accumulate in *CIT*$^{KI/KI}$ NPCs more frequently

resulting in a growth-arrested state in *CIT*$^{KI/KI}$ rosettes, while aNPCs progress more frequently to apoptosis in *CIT*$^{FS/FS}$ rosettes.

Discussion

In this study, we differentiate between the role of hypomorphic CIT-K signaling from *CIT* LOF defects in human and mouse brain development. The high frequency of binucleated neurons in mouse and human biallelic missense kinase inactive models indicates CIT-K's role in completion of cytokinesis is conserved between mouse and human models. However, this hypomorphic cytokinesis defect does not generate significant alterations in size, gross structure, or cytoarchitecture in Cit^{KIKI} mice as has been described for $Cit^{FS/FS}$ mice. These difference between the hypomorphic and LOF *Cit* mouse models underscores the shared human CIT^{KIKI} and $CIT^{FS/FS}$ phenotype of simplified neuroepithelium in neural rosettes, suggesting a human-specific role for CIT-K's catalytic activity in spatially organized cytokinesis, which is crucial for maintaining aNPC mitotic symmetry. The increased apoptosis in LOF neural tissues of both species highlights DNA damage-dependent apoptosis as a conserved determinant of brain size, which may explain the more severe microcephaly in *CIT* LOF models. The use of 3D brain organoids underscored a new role of CIT-K and its kinase-dependent developmental dynamics in polarized, pseudostratified cytoarchitecture that was not possible to study using 2D in vitro cultures. Together, these considerations further highlight human forebrain organoids derived from cells of affected individuals as a fundamental resource to study the impact of MCPH-associated pathogenic genetic variants on neurodevelopment.

Rodent models have been critical for uncovering the fundamental biology of corticogenesis and pathogenic mechanisms contributing to primary microcephaly (43). The *Flathead* rat and the *Cit*-knockout mouse phenocopy the severe microcephaly caused by human biallelic $CIT^{FS/FS}$ variants (23, 43). Affected animals

exhibit reduced brain size and cellularity, owing to failed cytokinesis, binucleated neural tissue, DNA damage, and apoptosis. Reduced brain size is preferentially attributed to elevated apoptosis, as inactivation of TP53 during *Cit*$^{FS/FS}$ brain development rescues this phenotype and results in a corresponding increase in binucleated neurons (18). Our data indicate this is a conserved pathogenic mechanism, with prolonged late M-phase, binucleation, and apoptosis observed in human *CIT*$^{FS/FS}$ organoids, corroborating in vivo data demonstrating the contribution of apoptosis to the pathogenic mechanism of microcephaly disorders (44). While microcephaly was not observed in the *Cit*$^{KI/KI}$ model, we show there is shared molecular pathology with other *CIT* models. Evidence of DNA damage accumulation and apoptosis were present, but to a lesser extent than in *Cit*$^{FS/FS}$ mice, suggesting there is a threshold that can be tolerated before apoptotic pathways profoundly impact brain size. In human brain organoids, prolonged cell cycle dynamics and elevated apoptosis were detected in *CIT*$^{KI/KI}$ organoids, but again to a lesser extent than in *CIT*$^{FS/FS}$ organoids. It is unclear if human brain development is more sensitive to the molecular consequences of hypomorphic CIT-K kinase activity, or if the increased duration of human gestation contributes to the *CIT*$^{KI/KI}$ microcephaly phenotype of affected individuals. Meanwhile, both human and mouse models indicate that CIT-K kinase functions are not fully redundant with scaffolding functions during cytokinesis.

The discovery that hypomorphic *CIT* alleles are the basis of primary microcephaly highlighted a previously unappreciated role for CIT-K kinase activity as a determinant of brain size (15). Human brain organoid models provided insight into the role of CIT-K kinase activity in corticogenesis and demonstrated the vulnerability

of the developing brain to cytokinesis defects. Reimagining of the same GFP-labeled *CIT*$^{KI/KI}$ and *CIT*$^{FS/FS}$ neural rosettes revealed a similar genotype-driven effect on cytoarchitecture integrity. Normally, polarized aNPCs attach to a small central lumen to form pseudostratified neural rosettes. In *CIT*-affected organoids, multiple neural rosettes progressively transform from a pseudostratified cytoarchitecture at 21DD to large lumens surrounded by a layer of cells resembling simple epithelial tissue at 28DD and 35DD. Similar cytoarchitecture defects in *CIT*$^{KI/KI}$ and *CIT*$^{FS/FS}$ neural rosettes indicates that CIT-K kinase activity is required to maintain the neuroepithelial polarity important for cortical morphogenesis as the cellular complexity of human neuroepithelium increases during development. The role of polarized cytokinesis of 3D aNPCs in neuroepithelium may explain the unique vulnerability of the developing brain to kinase disruption and implicate CIT-K kinase activity in coordinating this cell biology.

Polarized cytokinesis allows aNPCs to perpetuate their polarity (45, 46). Abscission at the apical border ensures precise distribution of fate determinants between daughter progeny. Moreover, abscission that occurs apically to newly formed cell-cell adhesion junctions between daughter and neighboring cells maintains attachment of progeny to the ventricular membrane/central lumen (45, 47). Lastly, apical endfeet, the aNPC membrane section that attaches to the central lumen, are divided to ensure each pseudostratified aNPC progeny has an apical contact as aNPCs divide symmetrically (45, 47). *CIT* organoids analyzed by live imaging and immunofluorescence showed increased frequency of misplaced midbodies relative to the apical border of the rosette central lumen and larger apical endfeet size in *CIT*$^{KI/KI}$ and *CIT*$^{FS/FS}$ neural rosettes, providing evidence that the fidelity of polarized

cytokinesis is disrupted in *CIT*-affected aNPCs. Alternatively, reduced cytoarchitectural complexity of *CIT*-affected neural rosettes could occur through premature differentiation due to altered fate determinant allocation and delamination of NPCs from the central lumen that do not form adhesion junctions in 3D tissue. These changes, effecting the number of cells connected to the apical surface, could also influence the size of the remaining apical endfeet. This pathology highlights an important role for polarized cytokinesis in cytoarchitectural complexity of pseudostratified neural rosettes.

Elegant studies in the *Drosophila* pupa epithelium demonstrated that coordination of cleavage furrow constriction of daughter cells requires neighbor membrane deformation and a focal disengagement of their E-cadherin adhesive contact (36). Likewise, daughter cells are ultimately integrated into epithelial tissue when midbody formation occurs in a polarized configuration relative to adhesion junction assembly. While this work exemplifies the role of cellular neighbors in successful completion of cytokinesis, it is also crucial that dividing cells “counteract” the cellular tension exerted by their neighbors to stabilize the midbody (48). Thus, polarity and/or tension relative to neighboring cells can change cytokinesis outcomes, highlighting the unique adaptations and vulnerabilities of cell division in 3D tissue. Data being generated from a diverse set of model systems are demonstrating that disrupting this cell biology can alter lumen size and epithelial organization, both of which are phenotypes in *CIT*-affected organoids (49, 50). These findings provide important insight for explaining the 2D in vitro versus 3D in vivo phenotypic discrepancies described in both human and mouse models and how it is that cytokinesis defects can impact epithelial organization and integrity. Similar considerations on 3D

cytoskeletal forces could be made in the study of CIT-K kinase molecular mechanisms in NPC genome integrity. Indeed all models showed an increased amount of DNA damage, recapitulating the clinical phenotype of affected individuals (30). In the future they could provide new insight about the role of MCPH genes in mechanisms linking cytoskeletal organization to genome integrity (51, 52).

CIT was the first of a growing list of genes, including *KIF14*, *CEP55,* and *PPP1R12A*, that encode components of cytokinesis machinery and are associated with severe brain size abnormalities (7). *KIF14* (OMIM ID: 611279) and *CEP55* (OMIM ID: 610000), like *CIT,* are recessively inherited etiologies of microcephaly, while variants in *PPP1R12A* (OMIM ID: 602021) are responsible for a *de novo* dominant form of a holoprosencephaly spectrum that includes individuals with microcephaly (53–55). These proteins share similar subcellular colocalization at the midbody and functional overlap during abscission, yet a single pathogenic mechanism is not evident. CEP55 localizes to the bulge of the midbody and recruits ESCRT machinery, a conserved membrane remodeling system used in severing midbody flanks during abscission (56). During mitosis, KIF14, a microtubule motor, accumulates at the spindle midzone, and localizes to the midbody in cells ready to undergo abscission (57). PPP1R12A accumulates at the central bulge of the midbody, regulates microtubule dynamics as a component of PP1β-MYPT1 phosphatase complex, and de-phosphorylates the centralspindlin complex kinesin component MKLP1 (58). Pathogenic variants in each gene are associated with highly penetrant features that severely affect the brain and some individuals also present with kidney abnormalities (53). Overall, with minimal impact on other organ systems, cytokinesis disorders punctuate the unique vulnerability of the developing brain to cytokinesis defects.

To better understand this unique vulnerability, several questions need to be answered. First, it is unknown which signaling pathways that coordinate cytokinesis are essential during brain development. Moreover, how the mammalian aNPC midbody forms at the apical membrane and interacts with cell junctions during cytokinesis and abscission has not been previously investigated in mouse or human models. These studies are further complicated by the limitations with evaluating the dynamics of cytokinesis cell biology in vivo. To tackle this problem, 3D live-cell imaging of sparsely labeled models can be used to track the long-term consequences of altering polarized cytokinesis. Finally, how the physical properties and composition of culture matrices, like Matrigel, constrain tissue and affect intracellular forces that impact 3D cytokinesis is yet to be determined. In conclusion, the identification and exploration of the aforementioned gaps in the field provide a compelling rationale for further research and investigation.

Materials and Methods

Sex as a biological variable

The iPSC lines used in this work were derived from male and female individuals (Figure 3) as previously published (15). Moreover, our study examined male and female animals, and similar findings are reported for both sexes.

Experimental animal work

The mouse strain containing the frameshift *Cit* LOF variant ($Cit^{FS/FS}$) in a C57BL/6 background was obtained from UC Davis KOMP repository ($Cit^{tm1a(KOMP)Wtsi}$). To generate CIT kinase inactive mice, we mutagenized *Cit*(c.376_377AA>GC; p.K126A) to generate the Lysine 126 to Alanine (K126A) substitution in the catalytic pocket in exon 3, using traditional ES cell-based knock-in technologies. This substitution totally inactivates the kinase domain and resembles pathogenic *CIT* variants found in affected individuals (14). We derived ES cell clones harboring the correct homologous recombination event. Heterozygous ($Cit^{+/KI}$) mice obtained from germline transmission of ES clones were intercrossed to generate homozygous ($Cit^{KI/KI}$) and control ($Cit^{+/+}$) progeny. Age-matched wild-type littermates were used as controls.

Behavioral characterization

The behavioral characterization of postnatal P8-P9 mice, including the evaluation of the maturity of ambulation, ataxic phenotype (i.e. spontaneous flipping on the back), vestibular reflexes and coordination (i.e. surface righting reflex and negative geotaxis on a 45° inclined surface), has been performed as described in (59). For the balance beam test, we used a wood beam with the following dimensions: 1cm wide, 100cm long, and suspended 12cm above the bench. Two-months old mice had to cross the beam to reach a cage enriched with toys. To familiarize the mice with the experimental

apparatus, thus reducing the animal stress, the experiment was preceded by 3 days of acclimation. On the day of the test, the animals were allowed to acclimate in the behavioral room at least 15 minutes before the experiment. Both *Cit*$^{KI/KI}$ and *Cit*$^{+/+}$ mice were tested individually, and each animal was encouraged to traverse the beam at least three times. The test was repeated for three consecutive days. The test was recorded using a video camera and analyzed offline by an operator blind to the genotype. The number of slips from the beam was measured to assess the motor performance.

In vitro kinase assay

Recombinant GST-MLC was obtained from bacteria expressing the corresponding expression vector (kind gift of Dr. Kozo Kaibuchi, Nagoya, Japan). Recombinant GST-CIT-SK (SK, short kinase) was obtained using the BD-Pharmingen (San Jose, CA, USA) baculovirus expression system by subcloning the mouse Cit-SK coding sequence (GeneBank accession no. AF086823) in the pAcG2T Transfer Vector. In both cases, GST fusion proteins were isolated from total cell lysates of bacterial and insect cells through Glutathione Sepharose 4B (GE Healthcare Lifesciences) affinity chromatography according to the manufacturer's specifications. For the in vitro kinase assay, recombinant proteins were incubated in 50µl of kinase buffer (50mM HEPES, pH 7.4, 5mM MgCl2, 3mM MnCl2, plus 0.1mM ATP and 10mCi of [γ-32P] ATP (6000 Ci/mM, Amersham) for 30 min at 30°C. The products were analyzed by 5 or 12.5% SDS-PAGE followed by autoradiography.

Western blotting

Tissues were lysed in RIPA buffer (1% NP40, 150 mmol/L of NaCl, 50 mmol/L of Tris-HCl pH 8, 5 mmol/L of EDTA, 0.01% SDS, 0.005% sodium deoxycholate, Roche protease inhibitors and PMSF) and homogenized in the same buffer with pellet

pestle (Z359971 Sigma-Aldrich). NPCs were washed two times with cold 1XPBS and then lysed with cold RIPA buffer. Cell lysates were collected and centrifuged at 14,000 x g at 4°C for fifteen minutes. For immunoblots, equal amounts of proteins from both whole-cell lysates were resolved by SDS–PAGE and blotted to nitrocellulose or PVDF membranes.

Mouse NPC isolation and culture

Embryonic brains were isolated from E12.5 timed pregnant mice. The lateral portion of the dorsal telencephalon was dissected, dissociated using a Papain-based kit, (Neural Tissue Dissociation Kit (P), Miltenyi Biotec, Bergisch Gladbach, Germany) and plated at the concentration of 5 x 10^4 cells/cm^2 on Poly-Lysine/Laminin-treated glass coverslips. Cells were analyzed 18h after plating. Culture medium comprised DMEM-F12, supplemented with 2% B27 w/o Retinoic Acid, 10 ng/mL EGF, and 40 ng/mL bFGF (all from Thermo Fisher Scientific, Waltham, MA). Cells were grown at 37° C in a humidified incubator with 5% CO2.

Staining of mouse embryonic cortex and adult mouse brain

Embryonic brains were dissected at E14.5 and fixed for 12-16 hours (h) at 4°C in 4% PFA. Postnatal mice were trans-cardially perfused with 4% PFA. After fixation, brains were equilibrated in 30% sucrose in PBS for 12-24h at 4°C, embedded with Tissue-TEK (O.C.T, Sakura Finetek, Alphen aan den Rijn, The Netherlands), frozen in liquid nitrogen, and stored at -20°C. Sectioning was then performed with a cryostat to obtain 20µm sections. Staining details can be found in the supplemental material.

Antibodies

The following antibodies were used: mouse monoclonal anti-CIT (#611377), mouse monoclonal anti-Ki67 (#550609) and mouse monoclonal anti N-Cadherin (#610920) from Transduction Laboratories, BD Biosciences (Franklin Lakes, NJ, USA). Mouse

monoclonal anti-vinculin (#V9131), mouse monoclonal anti-αTubulin (#T5168), rabbit polyclonal anti-Sox10 (HPA068898) from Sigma-Aldrich. Rabbit monoclonal anti-53BP1 (#ab36823), rabbit polyclonal anti-AuroraB (#ab2254) and mouse monoclonal anti-B-actin (#ab6276) from Abcam (Cambridge, UK). Rabbit polyclonal anti-cleaved Caspase 3 (#9661S), rabbit polyclonal anti-γH2AX (S139; 20E3; #2577) from Cell Signaling Technology. Rabbit polyclonal anti-BLBP (ABN14) from Millipore. Rat anti-BCL11B from Invitrogen (A48270). Mouse monoclonal anti-MKLP1 (sc-390113), goat polyclonal anti-DCX (sc-8066) from Santa Cruz Biotechnology. Mouse monoclonal anti-SOX2 (#MAB2018) from R&D Systems. Neuronal cells were detected by rabbit anti-Calbindin (1:1000, SWANT, CB-38a). Click-it TUNEL from Thermo Fisher (#C10619) was used for cell death detection in mice and organoids.

hPSC culturing

The iPSC lines used in this work were previously published in (15). Briefly, mycoplasma-free fibroblast lines from affected individuals, carrier individuals and healthy unrelated controls were episomally reprogramed. On average 15 iPSC lines were established from reprogramming of $1X10^6$ fibroblasts. 6 lines were expanded and characterized from each genotype. The pluripotent and genomic integrity of these lines were characterized for: morphology and growth rate, karyotype to rule out numerical and structural chromosomal abnormalities, and for the expression of pluripotency markers (NANOG, TRA-1-81, LIN28 and TRA-1-60). Low passage (p24) H9 hESCs (Lot#WB0090) were obtained from WiCell. Short tandem repeat analysis, sterility and quality tests were performed by WiCell. Chromosomal microarray confirmed that no hPSC line used had copy number variants associated with defined CNV syndromes based on the Decipher database. hPSCs were maintained in mTeSR1 medium (#85850, StemCell Technologies) on Matrigel-coated dishes (#354234, Corning) in a

cell incubator at 37°C with 5% CO2. Stem cells were chemically dissociated at 37°C using Versene (#15040066, Invitrogen) or mechanically dissociated, and then were resuspended in mTeSR1 with added Y27632 ROCK inhibitor (Tocris) at a final concentration of 10μM for 24 h to promote survival when cells were passaged. mTeSR1 medium was changed daily. Cells were not used past passage 50.

hESC *CIT*$^{FS/FS}$ generation by CRISPR/Cas9 genome editing

CIT$^{FS/FS}$ cell lines were generated by CRISPR/Cas9 genome editing to obtain a homozygous *CIT* frameshift genotype (*CIT* NM_007174.3: c.312_318del, p.C105Tfs*8) from newly thawed low passage H9 cells. A guide RNA expression vector was generated using annealed oligonucleotides (forward 5'-caccgtcagaagtcttgtaggttg-3' and reverse 5'-aaaccaacctacaagacttctgac-3') designed to target exon 4 of *CIT.* The annealed oligonucleotides were ligated into the Bbs1 restriction digested pX330. Subsequent transformation was accomplished using chemically competent Stbl3 E. coli (Invitrogen) and the cell suspension was plated on Lennox broth agar plates supplemented with ampicillin. Plates were incubated overnight for 16 hours at 37°C. Colonies were selected and inoculated into Lennox broth with ampicillin to be later extracted by Mini-prep (Qiagen). The extracted plasmids were screened with restriction digest and Sanger sequencing using the U6 forward primer 5'-gagggcctatttcccatgattcc-3'. Plasmids containing the insertions were further amplified and extracted using the Nucleobond Xtra Midi Plus EF kit (Macherey-Nagel) for experimental use. Electroporation was performed using the Lonza Human Stem Cell Nucleofector Kit 2 (Lonza) according to manufacturer's instructions. Electroporated cells were transferred to a Matrigel-coated dish containing mTeSR1 supplemented with Y27632 ROCK inhibitor (Tocris) and Normocin (InvivoGen). A few days later, cells were then diluted into Matrigel-coated

96-well plates for screening. Wells with individual colonies were screened by Sanger sequencing using primers to amplify exon 4 of *CIT* (forward 5'-tggggctaactcttgcatct-3' and reverse 5'-cactccggtacagaaagtgga-3'). Edited lines were analyzed by chromosomal microarray to affirm genomic integrity and Western blot to confirm the absence of CIT-K protein expression.

Generation of hPSCs with stable expression of Lifeact-GFP and H2B-mCherry fluorescent reporters

hPSCs were stably labeled with H2B-mCherry and Lifeact-GFP using the PiggyBac transposase method, which allows for random genomic integration of DNA sequences containing inverted terminal repeat sequences (34). hPSCs were transfected at a low passage number using Lipofectamine Stem reagent (Invitrogen) and Opti-MEM I Reduced Serum medium (Invitrogen). Three plasmids were transfected at equal parts: pCAG:H2B-Cherry, pCAG:Lifeact-GFP, and pCAG:PBase expressing the PiggyBac transposase, provided by Dr. Orly Reiner at the Weizmann Institute of Science. Mechanical passaging was used to select for cells expressing both H2B-mCherry and Lifeact-GFP.

Neural differentiation

hPSCs were differentiated to NPCs and dorsal forebrain organoids using dual inhibition of SMAD signaling as previously described (31). The following media were used during the differentiation protocol:

- N2 + Dual SMAD inhibition medium: 1:100 N2 supplement (#17502048 ThermoFisher), 1μM Dorsomorphin (Tocris), 2μM A83-01 (Tocris) in DMEM/F12 (#11320033, Gibco).

- N2 + B27 + Dorsomorphin medium: 1:200 N2 supplement, 1:100 B27 supplement (#17504044 ThermoFisher), 1µM Dorsomorphin, 20ng/mL bFGF in DMEM/F12.
- N2 + B27 medium: 1:200 N2 supplement, 1:100 B27 supplement, 20ng/mL bFGF in DMEM/F12

Generation and maintenance of hPSC aggregates (0-7DD)

hPSCs were chemically dissociated at 37°C using Versene or StemPro™ Accutase™ Cell Dissociation Reagent (#A1110501, Gibco) and resuspended in mTeSR1 with added Y27632 ROCK inhibitor at a final concentration of 10µM. Cells were counted and diluted to a concentration of $2x10^4$ cells per ml. 30µL of the cell suspension, containing approximately 600 cells, was dispensed in each well of an ultra-low cell attachment 96-well plate with a V-shaped bottom (#MS-9096VZ S-Bio) to encourage cell aggregation. This step is considered day 0 of differentiation (0DD). Neural induction was initiated 36 hours later (1.5DD) by adding 150µL of N2 + dual SMAD inhibition medium to each well, and on 3DD aggregates were transferred to ultra-low cell attachment 6-well plates to continue growth in suspension. Media was changed every 48 hours. Aggregates were inserted into pre-constructed compartments at 7DD.

Construction of microfabricated devices, assembly and confocal analysis

Device fabrication and assembly were adapted from established protocols (35, 60). Details can be found in the supplemental material. Confocal imaging was conducted on days 21, 28, and 35DD using a Nikon X1 Yokogawa spinning disk confocal and a Tokai Hit incubated stage to maintain device incubation. Details can be found in the supplemental material.

NPCs isolation and organoids growth in suspension

hPSC aggregates were generated and maintained (0-7DD) as previously described. On 7DD, medium was changed to N2 + B27 + Dorsomorphin and aggregates were transferred to a 6-well plate (Corning) coated with Matrigel using a 200µL pipette with a razor cut tip to minimize shearing forces on the aggregates (~ 12-15 aggregates per well). Extra media was then added to reach 2mL of N2 + B27 + Dorsomorphin per well. Media was changed every 48 hours. On 14DD, NPCs were generated by gently detaching neural rosettes from Matrigel using a p200 tip, followed by chemical dissociation using Accutase (Invitrogen). Dissociated cells were plated on 15µg/mL poly-L-ornithine (Sigma) and 10µg/mL laminin (Sigma) coated dishes. For dorsal forebrain organoid generation, neural rosettes were gently detached from Matrigel using a p200 tip and the neural tissue was grown in suspension under constant rotation at 95 rpm. The N2 + B27 medium was implemented on 14DD with a medium change every other day until 35DD.

Organoid cryopreservation, embedding, and sectioning

Organoids were fixed in 4% PFA overnight before beginning cryopreservation. Organoids were saturated in a 15% sucrose solution overnight or until tissue sank to the bottom of a conical tube before applying the final 30% sucrose solution. Once tissue was sufficiently cryopreserved, the organoids were placed in a plastic cassette containing OCT medium (Fisher Brand) and frozen using -60°C to -70°C 2-methyl butane. OCT-containing organoid blocks were sectioned at 13µm using a cryostat (Leica Biosystems).

Immunofluorescence on organoids

13µm cryopreserved sections of cerebral organoid tissue adhered on slides (Fisher Brand) were used for immunofluorescence. A subset of slides to be stained with CIT, MKLP1, BCL11B, Cleaved Caspase 3, or yH2AX were treated with sodium citrate

(10mM) antigen retrieval prior to staining methods. Slides were washed three times with 1xPBS for five minutes. Tissue was then permeabilized with 0.1% Triton X-100 for five minutes, and subsequently washed once with 1xPBS for five minutes before blocking buffer was implemented. Organoid sections were incubated with blocking buffer (0.1% Triton X-100, 1% BSA, and 5% NDS) for one-hour at room temperature. Primary antibodies were diluted in blocking buffer and incubated at 4°C overnight. Sections were then exposed for 1-2 h at room temperature to secondary antibodies conjugated with Alexa-Fluor (Invitrogen) and finally incubated with Hoechst (Invitrogen) diluted at 1:10,000 in PBS for five minutes. Coverslips were mounted on the glass slides using Prolong Gold (Invitrogen) overnight before imaging.

Image processing and data analysis

Details can be found in the supplemental material file.

Statistics

Statistical analyses were performed using Microsoft Office Excel (Version 16, Microsoft Corporation, Redmond, WA, USA) and GraphPad (Version 10, GraphPad Software, San Diego, CA, USA). Unpaired two-tailed Student's *t*-test was used to compare two groups and One-way or Two-way ANOVA test were used for multiple group comparisons followed by Bonferroni or Holm-Sidak post-hoc analysis. Mann-Whitney test was used to analyze γH2AX and 53BP1 foci, and time spent from anaphase to G1 ascension during cell division. The Fisher Exact Probability Test was used for percentage distribution. Data are shown as the mean values of at least 3 independent experiments and standard error of the mean (mean ± SEM). *P<0.05,**P<0.01, ***P<0.001, ****P<0.0001.

Study approval

For iPSC lines, subjects were enrolled according to protocols approved by institutional review boards at affiliated institutions, as previously described (15). In all cases, the procedures followed were in accordance with the ethical standards of the respective institution's committee on human research and were in keeping with international standards. Written informed consent was obtained prior to participation. The animal studies were designed according to the guidelines of the NIH, the European Communities Council (2010/63/EU) and the Italian Law for Care and Use of Experimental Animals (DL26/2014), under permission number 1128/2020-PR, released on 16th November 2020 from Italian Ministry of Health, Department of Public Veterinary Health. It was also approved by the Italian Ministry of Health and the Bioethical Committee of the University of Turin.

Data availability

The original contributions presented in the study are included in the article and supplementary material. Supporting data values associated with the main article and supplemental material are included in the Supporting Data Values Excel (XLS) file, with separate tabs for each applicable figure panel. Further inquiries can be directed to the corresponding authors.

Author contributions

Conception and design: GP, AM, FDC, SLB; Development of methodology: AM, GP , FB, ET, OR and RYT; Acquisition of data: GP, AM, GI, RP, ERP, AF, GEB, EB, ML, SS, HFM, SW, NG, MC, JE; Analysis of data: GI, AM, GP, ERP, EB; Data interpretation, GP, AM, GI, ERP, EB, OR, AB, FDC, SLB; Writing of the manuscript: GP, AM, GI, ERP, FDC, SLB; All authors contributed to the article and approved the submitted version. GP is the first author in the list of shared first authors, as he initiated the project and performed animal experiments. AM is the second author in the list of

shared first authors, as she initiated the project and performed the majority of the organoid experiments. GI is the third author in the list of shared first authors, as she completed the analysis to bring this manuscript to completion.

Acknowledgments

We thank Dr. David Burke for his technical assistance in constructing microfabricated imaging hardware. This work was supported by the Eunice Kennedy Shriver National Institute of Child Health and Human development (R01AWD010411 to SLB), National Institute of Neurological Disorders and Stroke (R01NS101597 to SLB), Khan CVC Michigan-Israel Partnership Grant (SLB and OR), Michigan Pre-doctoral Training Program in Genetics (T32-GM007544 to AM), Global Research Engagement Opportunity Award (to AM), Endowment for the Development of Graduate Education Award (to AM), Neuroscience training grant (T32-NS076401 to ERP). The laboratory of FDC was supported by Associazione Italiana per la Ricerca sul Cancro (AIRC) with grant IG23341 and PRIN-PNRR project n. 2022M75NN8 from Italian Ministry of University and Research. GP was supported by a fellowship from AIRC. The contribution of Cassa di Risparmio di Torino (CRT) and of University of Torino ex-60% fund to FDC are also gratefully acknowledged. GI and AF were supported by a PhD fellowship from the Italian Ministry of University and Research (MIUR). EB was supported by Telethon Foundation grant #GMR22T1066 (Telethon Multiround 21-24 – Round 1 2022 Track Basic).

References

1. Vaid S, Huttner WB. Progenitor-Based Cell Biological Aspects of Neocortex Development and Evolution. *Front Cell Dev Biol*. 2022;10:892922.

2. Miller DJ, et al. Shared and derived features of cellular diversity in the human cerebral cortex. *Curr Opin Neurobiol*. 2019;56:117–124.

3. Villalba A, Götz M, Borrell V. The regulation of cortical neurogenesis. *Curr Top Dev Biol*. 2021;142:1–66.

4. Espinós A, et al. Evolution of genetic mechanisms regulating cortical neurogenesis. *Dev Neurobiol*. 2022;82(5):428–453.

5. Götz M, Huttner WB. The cell biology of neurogenesis. *Nat Rev Mol Cell Biol*. 2005;6(10):777–788.

6. Hakanen J, Ruiz-Reig N, Tissir F. Linking Cell Polarity to Cortical Development and Malformations. *Front Cell Neurosci*. 2019;13:244.

7. Jayaraman D, Bae B-I, Walsh CA. The Genetics of Primary Microcephaly. *Annu Rev Genomics Hum Genet*. 2018;19:177–200.

8. Jean F, Stuart A, Tarailo-Graovac M. Dissecting the Genetic and Etiological Causes of Primary Microcephaly. *Front Neurol*. 2020;11:570830.

9. Phan TP, Holland AJ. Time is of the essence: the molecular mechanisms of primary microcephaly. *Genes Dev*. 2021;35(23–24):1551–1578.

10. Parry DA, et al. Heterozygous lamin B1 and lamin B2 variants cause primary microcephaly and define a novel laminopathy. *Genet Med*. 2021;23(2):408–414.

11. Tingler M, Philipp M, Burkhalter MD. DNA Replication proteins in primary microcephaly syndromes. *Biol Cell*. 2022;114(6):143–159.

12. Pulvers JN, et al. Mutations in mouse Aspm (abnormal spindle-like microcephaly associated) cause not only microcephaly but also major defects in the germline. *Proc*

Natl Acad Sci U S A. 2010;107(38):16595–16600.

13. Chen J-F, et al. Microcephaly disease gene Wdr62 regulates mitotic progression of embryonic neural stem cells and brain size. *Nat Commun*. 2014;5:3885.

14. Harding BN, et al. Mutations in Citron Kinase Cause Recessive Microlissencephaly with Multinucleated Neurons. *Am J Hum Genet*. 2016;99(2):511–520.

15. Li H, et al. Biallelic Mutations in Citron Kinase Link Mitotic Cytokinesis to Human Primary Microcephaly. *Am J Hum Genet*. 2016;99(2):501–510.

16. D'Avino PP. Citron kinase - renaissance of a neglected mitotic kinase. *J Cell Sci*. 2017;130(10):1701–1708.

17. Bianchi FT, et al. Of rings and spines: The multiple facets of Citron proteins in neural development. *Small GTPases*. 2017;11(2):122–130.

18. Bianchi FT, et al. Citron Kinase Deficiency Leads to Chromosomal Instability and TP53-Sensitive Microcephaly. *Cell Rep*. 2017;18(7):1674–1686.

19. Madaule P, et al. Role of citron kinase as a target of the small GTPase Rho in cytokinesis. *Nature*. 1998;394(6692):491–494.

20. Gai M, et al. ASPM and CITK regulate spindle orientation by affecting the dynamics of astral microtubules. *EMBO Rep*. 2016;17(10):1396–1409.

21. Shaheen R, et al. Mutations in CIT, encoding citron rho-interacting serine/threonine kinase, cause severe primary microcephaly in humans. *Hum Genet*. 2016;135(10):1191–1197.

22. Basit S, et al. CIT, a gene involved in neurogenic cytokinesis, is mutated in human primary microcephaly. *Hum Genet*. 2016;135(10):1199–1207.

23. Di Cunto F, et al. Defective neurogenesis in citron kinase knockout mice by altered cytokinesis and massive apoptosis. *Neuron*. 2000;28(1):115–127.

24. Sarkisian MR, et al. Citron-kinase, a protein essential to cytokinesis in neuronal progenitors, is deleted in the flathead mutant rat. *J Neurosci*. 2002;22(8):RC217.
25. Doyle A, et al. The construction of transgenic and gene knockout/knockin mouse models of human disease. *Transgenic Res*. 2012;21(2):327–349.
26. Di Cunto F, et al. Citron rho-interacting kinase, a novel tissue-specific ser/thr kinase encompassing the Rho-Rac-binding protein Citron. *J Biol Chem*. 1998;273(45):29706–29711.
27. Camera P, et al. Citron-N is a neuronal Rho-associated protein involved in Golgi organization through actin cytoskeleton regulation. *Nat Cell Biol*. 2003;5(12):1071–1078.
28. Camera P, et al. The RhoA-associated protein Citron-N controls dendritic spine maintenance by interacting with spine-associated Golgi compartments. *EMBO Rep*. 2008;9(4):384–392.
29. Dwyer ND, et al. Neural Stem Cells to Cerebral Cortex: Emerging Mechanisms Regulating Progenitor Behavior and Productivity. *J Neurosci*. 2016;36(45):11394–11401.
30. Boda E, et al. Molecular and functional heterogeneity in dorsal and ventral oligodendrocyte progenitor cells of the mouse forebrain in response to DNA damage. *Nat Commun*. 2022;13(1):2331.
31. Chambers SM, et al. Highly efficient neural conversion of human ES and iPS cells by dual inhibition of SMAD signaling. *Nat Biotechnol*. 2009;27(3):275–280.
32. Di Lullo E, Kriegstein AR. The use of brain organoids to investigate neural development and disease. *Nat Rev Neurosci*. 2017;18(10):573–584.
33. Johnson CA, Wright CE, Ghashghaei HT. Regulation of cytokinesis during corticogenesis: focus on the midbody. *FEBS Lett*. 2017;591(24):4009–4026.

34. Wu SC-Y, et al. piggyBac is a flexible and highly active transposon as compared to sleeping beauty, Tol2, and Mos1 in mammalian cells. *Proc Natl Acad Sci U S A*. 2006;103(41):15008–15013.

35. Karzbrun E, Tshuva RY, Reiner O. An On-Chip Method for Long-Term Growth and Real-Time Imaging of Brain Organoids. *Curr Protoc Cell Biol*. 2018;81(1):e62.

36. Herszterg S, et al. Interplay between the dividing cell and its neighbors regulates adherens junction formation during cytokinesis in epithelial tissue. *Dev Cell*. 2013;24(3):256–270.

37. Hatte G, Prigent C, Tassan J-P. Adherens junctions are involved in polarized contractile ring formation in dividing epithelial cells of Xenopus laevis embryos. *Exp Cell Res*. 2021;402(1):112525.

38. Casas Gimeno G, Paridaen JTML. The Symmetry of Neural Stem Cell and Progenitor Divisions in the Vertebrate Brain. *Front Cell Dev Biol*. 2022;10:885269.

39. Gai M, et al. Citron kinase controls abscission through RhoA and anillin. *Mol Biol Cell*. 2011;22(20):3768–3778.

40. Pallavicini G, et al. Inactivation of Citron Kinase Inhibits Medulloblastoma Progression by Inducing Apoptosis and Cell Senescence. *Cancer Res*. 2018;78(16):4599–4612.

41. Pallavicini G, et al. CITK Loss Inhibits Growth of Group 3 and Group 4 Medulloblastoma Cells and Sensitizes Them to DNA-Damaging Agents. *Cancers (Basel)*. 2020;12(3):542.

42. Kari S, et al. Programmed cell death detection methods: a systematic review and a categorical comparison. *Apoptosis*. 2022;27(7–8):482–508.

43. Roberts MR, et al. The flathead mutation causes CNS-specific developmental abnormalities and apoptosis. *J Neurosci*. 2000;20(6):2295–2306.

44. Iegiani G, et al. The impact of TP53 activation and apoptosis in primary hereditary microcephaly. *Front Neurosci*. 2023;17:1220010.

45. McNeely KC, Dwyer ND. Cytokinetic Abscission Regulation in Neural Stem Cells and Tissue Development. *Curr Stem Cell Rep*. 2021;7(4):161–173.

46. Yang X, et al. Stepwise maturation of apicobasal polarity of the neuroepithelium is essential for vertebrate neurulation. *J Neurosci*. 2009;29(37):11426–11440.

47. Buckley CE, St Johnston D. Apical-basal polarity and the control of epithelial form and function. *Nat Rev Mol Cell Biol*. 2022;23(8):559–577.

48. Founounou N, Loyer N, Le Borgne R. Septins regulate the contractility of the actomyosin ring to enable adherens junction remodeling during cytokinesis of epithelial cells. *Dev Cell*. 2013;24(3):242–255.

49. Luján P, et al. PRL-3 disrupts epithelial architecture by altering the post-mitotic midbody position. *J Cell Sci*. 2016;129(21):4130–4142.

50. Veeraval L, O'Leary CJ, Cooper HM. Adherens Junctions: Guardians of Cortical Development. *Front Cell Dev Biol*. 2020;8:6.

51. Kim JM. Molecular Link between DNA Damage Response and Microtubule Dynamics. *Int J Mol Sci*. 2022;23(13):6986.

52. Iegiani G, Di Cunto F, Pallavicini G. Inhibiting microcephaly genes as alternative to microtubule targeting agents to treat brain tumors. *Cell Death Dis*. 2021;12(11):1–11.

53. Hughes JJ, et al. Loss-of-Function Variants in PPP1R12A: From Isolated Sex Reversal to Holoprosencephaly Spectrum and Urogenital Malformations. *Am J Hum Genet*. 2020;106(1):121–128.

54. Frosk P, et al. A truncating mutation in CEP55 is the likely cause of MARCH, a novel syndrome affecting neuronal mitosis. *J Med Genet*. 2017;54(7):490–501.

55. Barrie ES, et al. Expanding the spectrum of CEP55-associated disease to viable phenotypes. *Am J Med Genet A*. 2020;182(5):1201–1208.

56. Little JN, Dwyer ND. Cep55: abscission boss or assistant? *Trends Cell Biol*. 2021;31(10):789–791.

57. Gruneberg U, et al. KIF14 and citron kinase act together to promote efficient cytokinesis. *J Cell Biol*. 2006;172(3):363–372.

58. Capalbo L, et al. The midbody interactome reveals unexpected roles for PP1 phosphatases in cytokinesis. *Nat Commun*. 2019;10(1):4513.

59. Feather-Schussler DN, Ferguson TS. A Battery of Motor Tests in a Neonatal Mouse Model of Cerebral Palsy. *J Vis Exp*. 2016;(117):53569.

60. Karzbrun E, et al. Human Brain Organoids on a Chip Reveal the Physics of Folding. *Nat Phys*. 2018;14(5):515–522.

Figure legends

<u>Figure 1</u> *Cit*$^{KI/KI}$ mice show grossly normal CNS morphological structure with an ataxic phenotype

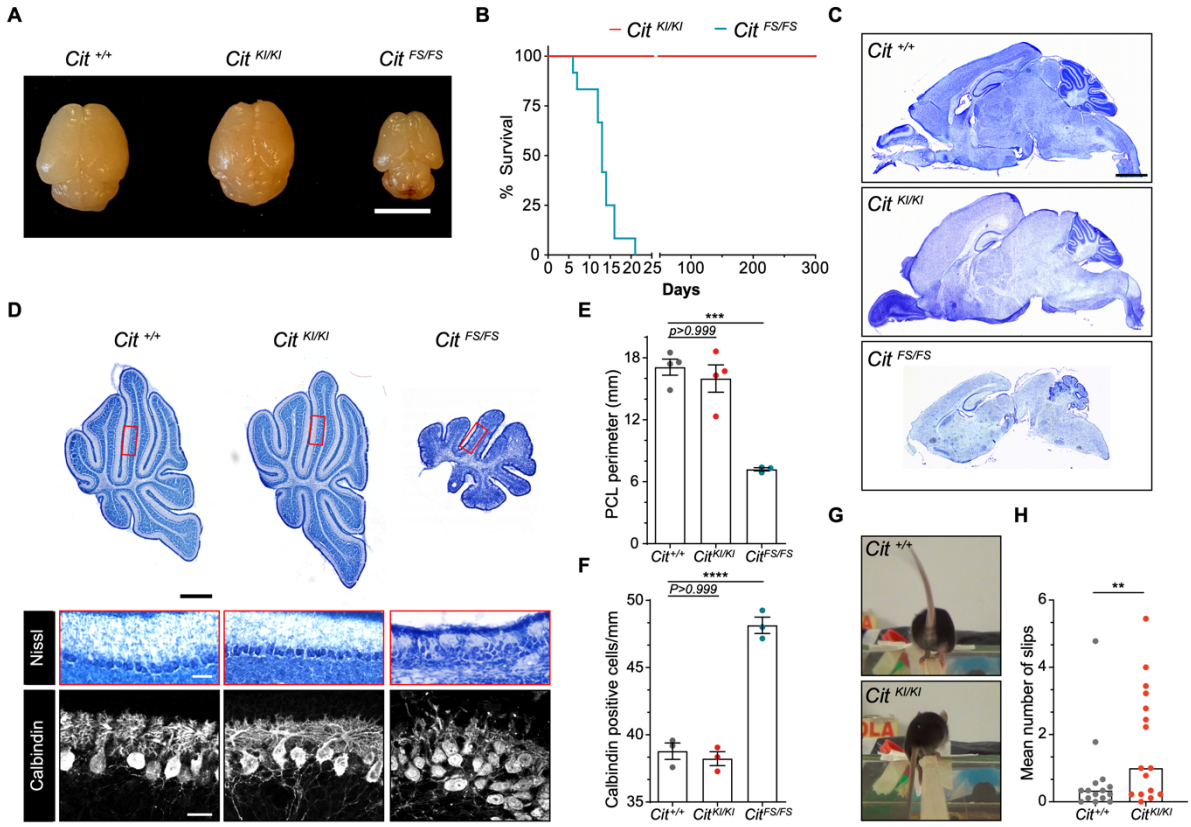

(**A**) Representative picture of *Cit* $^{+/+}$, *Cit*$^{KI/KI}$ and *Cit*$^{FS/FS}$ P10 brains. Scale bar = 5mm

(**B**) Kaplan–Meier survival curves of *Cit*$^{KI/KI}$ (N=12) mice compared to *Cit*$^{FS/FS}$ (N=12). Log-rank (Mantel–Cox) test was used to compare survival between experimental groups (****P<0.0001).

(**C**) Cresyl Violet staining of sagittal sections of *Cit* $^{+/+}$, *Cit*$^{KI/KI}$ and *Cit*$^{FS/FS}$ P10 brains. Scale bar = 1mm

(**D**) Upper panel: Cresyl Violet staining of sagittal sections from the midline (vermis) of *Cit* $^{+/+}$, *Cit*$^{KI/KI}$ and *Cit*$^{FS/FS}$ P10 cerebella showing the anterior, central and the posterior sector. Scale bar = 500µm. Middle panel: high magnification Nissl stain of lobule V inset from the midline (vermis). Scale bar = 50µm. Lower panel:

immunofluorescence analysis for the Purkinje Cell marker Calbindin1 (Calbindin), of sagittal sections of lobule V from the midline (vermis) obtained from P10 mice. Scale bar =25µm

(**E**) Quantification of Purkinje cell layer (PCL) perimeter in the vermis of P10 *Cit* $^{+/+}$, *Cit*$^{KI/KI}$ and *Cit*$^{FS/FS}$ mice.

(**F**) Quantification of Purkinje cell density per mm in the vermis of *Cit* $^{+/+}$, *Cit*$^{KI/KI}$ and *Cit*$^{FS/FS}$ P10 mice. Purkinje cells were stained for Calbindin1 (Calbindin).

(**G**) Representative picture extracted from videos of *Cit*$^{+/+}$ and *Cit*$^{KI/KI}$ mice slipping during beam walking test.

(**H**) Quantification of the mean number of slips for 3 consecutive days of the beam walking test on the same animal.

Error bars, SEM. **P<0.01, ***P<0.001; one-way ANOVA test followed by Bonferroni's post-hoc analysis (E and F), unpaired Student's t-test (H). Each dot represents an independent animal.

<u>Figure 2</u> *Cit*$^{KI/KI}$ mice show increased apoptosis, DNA damage, and cytokinesis failure in CNS tissue, but less than *Cit*$^{FS/FS}$ mice

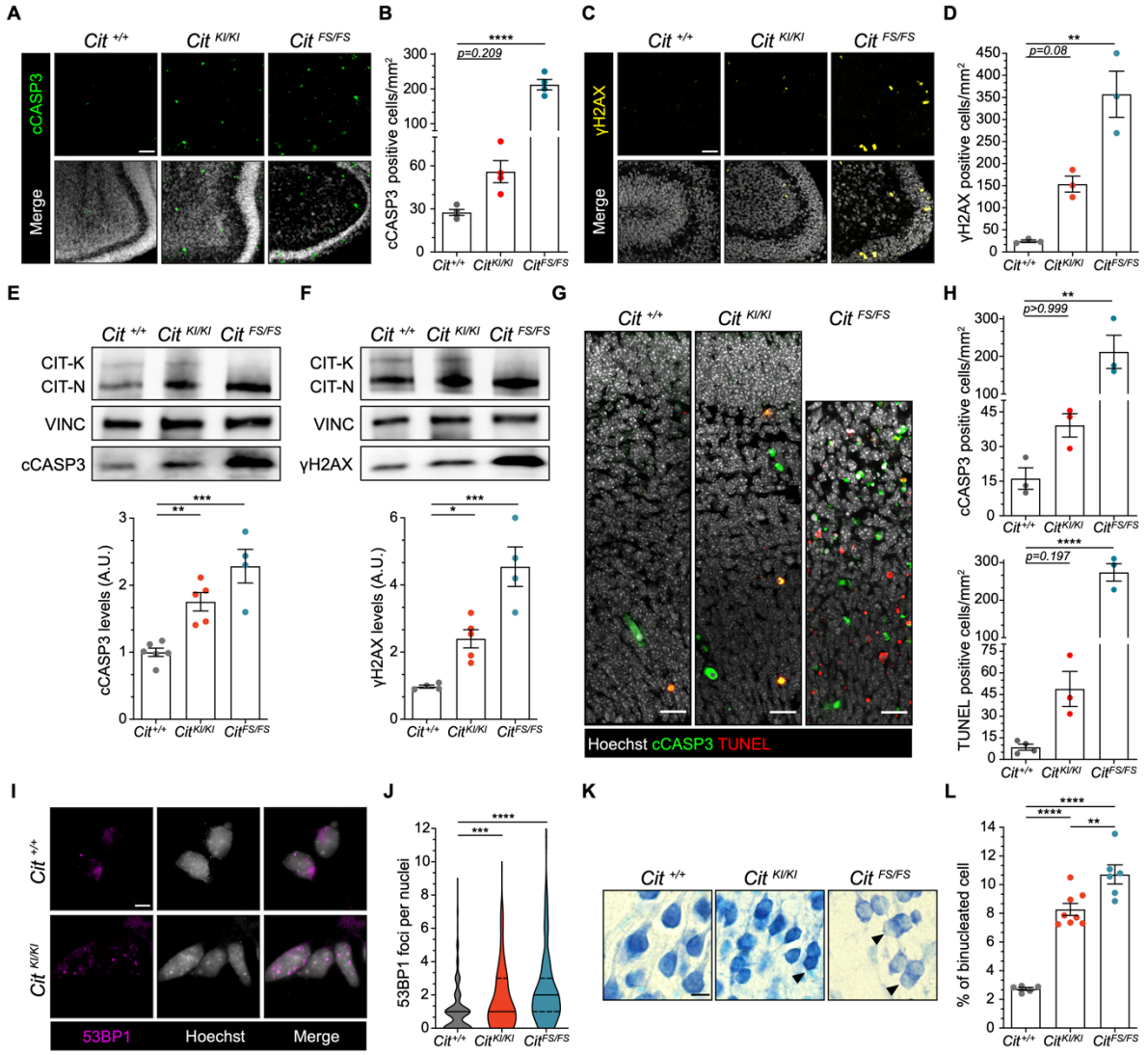

(**A**) Immunofluorescence analysis of P4 cerebella from mice of the indicated genotypes for apoptotic marker cCASP3 (green) and Hoechst (gray). Scale bars = 25μm.

(**B**) Quantification of cCASP3 positive cells in (A).

(**C**) Immunofluorescence analysis of P4 cerebella from mice of the indicated genotypes for DNA damage marker γH2AX (yellow) and Hoechst (gray). Scale bars = 25μm.

(**D**) Quantification of γH2AX positive cells in (C).

(**E-F**) Western blot analysis of total lysate from P4 cerebella from mice of the indicated genotypes. The levels of cCASP3 (E) and γH2AX (F) were analyzed based on at least three independent biological replicates and the internal loading control was vinculin (VINC). A.U. = arbitrary unit.

(**G**) Immunofluorescence analysis for apoptotic marker cCASP3 (green), TUNEL assay (red), and Hoechst (gray) of E14.5 cortex obtained from embryos of the indicated genotypes. Scale bars =10μm.

(**H**) Quantification of cCASP3 and TUNEL-positive cells in (G).

(**I**) Representative images of E12.5 NPCs from *Cit* $^{+/+}$ and *Cit* $^{KI/KI}$ embryos, immunostained for 53BP1 (magenta) and Hoechst (gray) 24 hours after plating. Scale bars=10 μm.

(**J**) Quantification of 53BP1 nuclear foci in (I); >250 cells were counted for each genotype in each replicate (n=3).

(**K**) High-power fields of Cresyl Violet stained coronal sections of P10 cortex obtained from mice of the indicated genotypes. Black arrowheads indicate binucleated cells. Scale bars=10μm.

(**L**) Quantification of binucleated cells in (K).

In microscopy quantifications, every dot represents an independent animal and at least 9 fields per genotype were analyzed. Error bars, SEM. *P<0.05, **P<0.01,***P<0.001, ****P<0.0001; one-way ANOVA test followed by Holm-Sidak post-hoc analysis.

Figure 3 Modeling *CIT* variants using human models of neurodevelopment

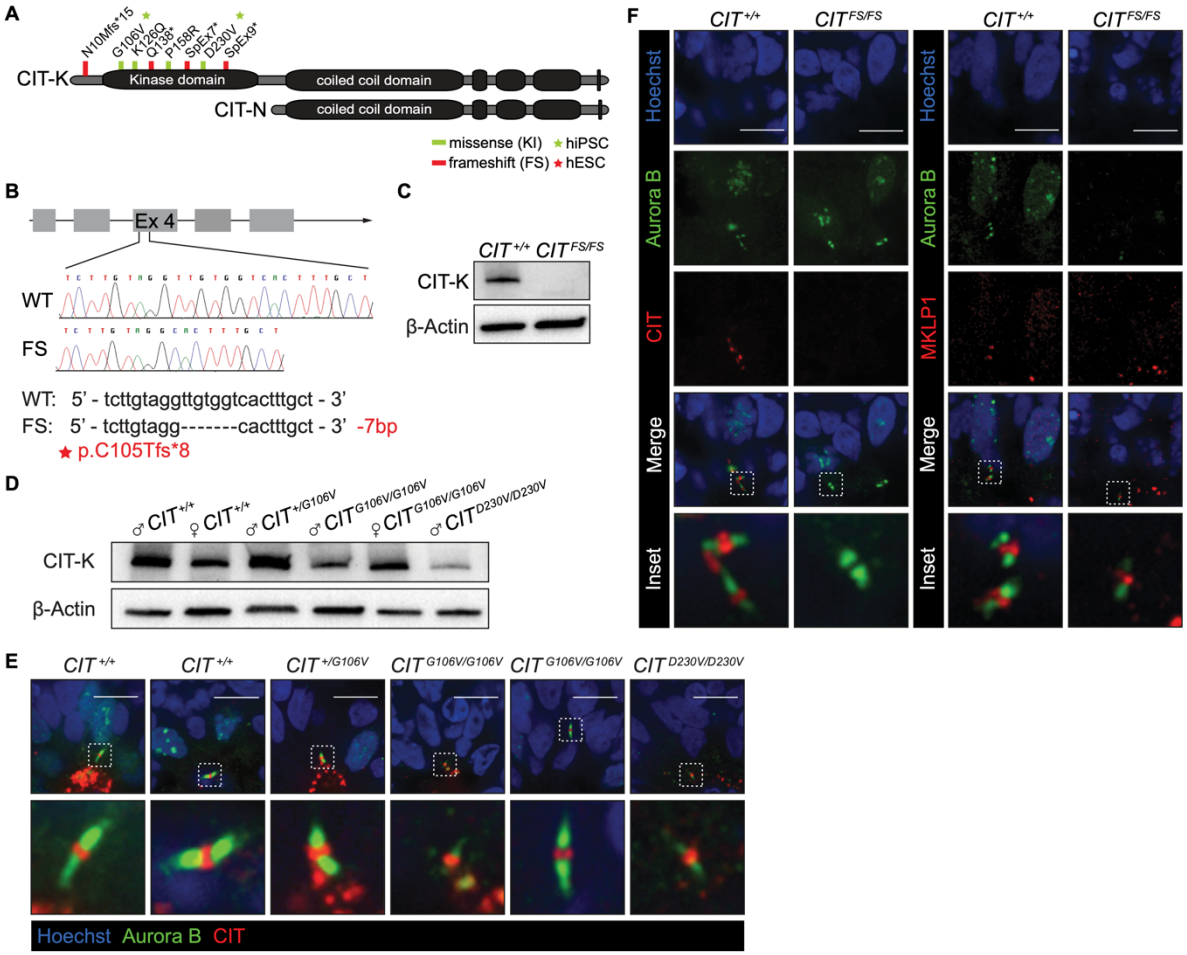

(**A**) Scheme of CIT-K and CIT-N protein isoforms. Homozygous and compound heterozygous variants localize in the N-terminus and within the kinase domain of CIT-K. Missense variants depicted in green, and LOF frameshift and splice variants depicted in red.

(**B**) CRISPR/Cas9-mediated targeting of the *CIT* locus at exon 4. Sequences and chromatograms of the seven-base pair deletion are shown with the corresponding alteration to protein sequence highlighted in red.

(**C**) Western blot analysis of CIT expression in NPCs of indicated genotypes. CIT-K isoform is absent in CRISPR/Cas9-edited *CIT*$^{FS/FS}$ line.

(**D**) Western blot analysis of CIT expression in NPCs of the indicated genotypes. Variability in CIT-K abundance detected in *CIT*$^{KI/KI}$ NPCs compared to unaffected controls.

(**E**) Immunofluorescence for Aurora B (green) midbody arms and CIT (red) shows presence of CIT in the midbody central bulge in indicated genotypes of 35DD dorsal forebrain organoids. Scale bars =10μm

(**F**) Immunofluorescence for Aurora B (green) midbody arms and midbody central bulge markers CIT (red) or MKLP1 (red) in 35DD dorsal forebrain organoids. CIT is absent in the midbody central bulge in *CIT*$^{FS/FS}$ 35DD organoids. Immunofluorescence with midbody central bulge marker MKLP1 (red) shows presence of this structure flanked by Aurora B (green) midbody arms in *CIT*$^{FS/FS}$ 35DD organoids. Scale bars =10μm

<u>Figure 4</u> *CIT* affected organoids demonstrate changes to pseudostratified neuroepithelium

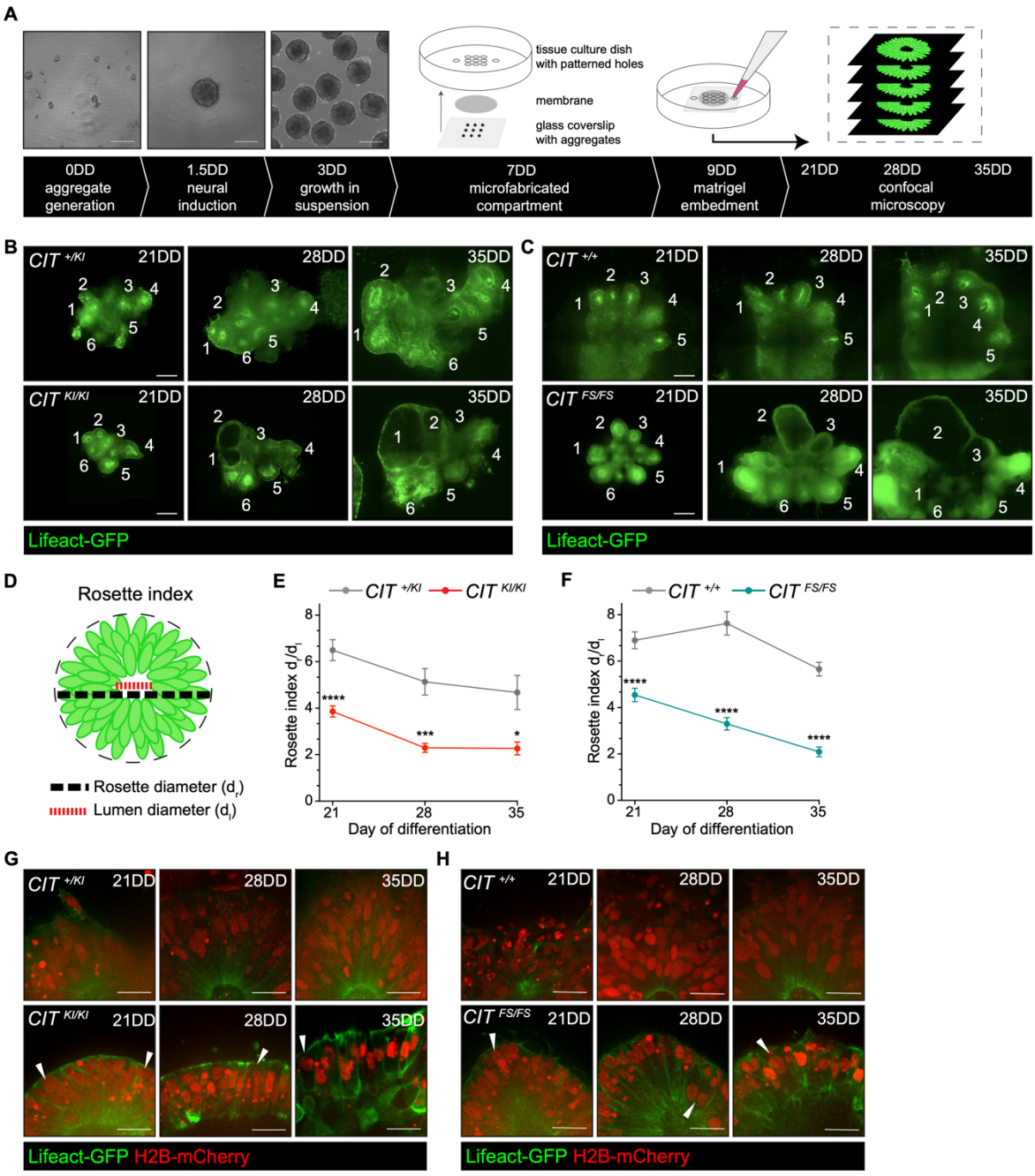

(**A**) Schematic of dorsal forebrain organoid differentiation and microfabricated compartment generation with corresponding time stamps. Neural differentiation begins with hPSC aggregate generation at 0DD, followed by neural induction at 1.5DD. An illustration of the microfabricated compartment depicts the orientation of

compartment components. Neural aggregates are positioned on glass coverslips in a 3x3 pattern at 7DD, and the compartment is sealed with a UV adhesive. Neural differentiation medium fills the tissue culture dish to facilitate medium and gas exchange to the compartment containing the developing tissue. Two days later, on 9DD, the compartment is embedded with Matrigel. Inverted confocal microscopy is performed at the compartment coverslip on 21DD, 28DD, and 35DD. Scale bar = 200μm

(**B-C**) Representative images of developing organoids and rosettes (white numbers) across time using Lifeact-GFP. Affected *CIT*$^{FS/FS}$ and *CIT*$^{KI/KI}$ rosettes exhibit large lumens and a reduction in neuroepithelial complexity. Scale bars = 250μm

(**D**) Illustration of rosette measurements performed across *CIT* organoids. Diameter measurements and R_i calculations across organoid rosettes.

(**E-F**) Quantification of rosette index (d_r / d_l) in *CIT*$^{+/KI}$ and in *CIT*$^{KI/KI}$ organoids (E) and in *CIT*$^{+/+}$ and in *CIT*$^{FS/FS}$ organoids (F).

(**G-H**) Representative insets of developing rosettes across time using Lifeact-GFP and H2B-mCherry. Control rosettes maintain a pseudostratified neuroepithelium at all three time points, while many affected *CIT*$^{KI/KI}$ and *CIT*$^{FS/FS}$ rosettes demonstrate a transition towards a simple epithelial architecture. Multinucleated cells are apparent in the rosette and examples are shown (white arrowheads). Scale bars = 25μm

Quantification from a minimum of two independent compartment preparations per genotype. Compartments each contain ≤ 9 organoids per preparation. Error bars, SEM. ***P <0.001, ****P <0.0001 by Repeated measures two-way ANOVA.

<u>Figure 5</u> *CIT* affected organoids show aNPC apical endfeet area increases and mitotic defects

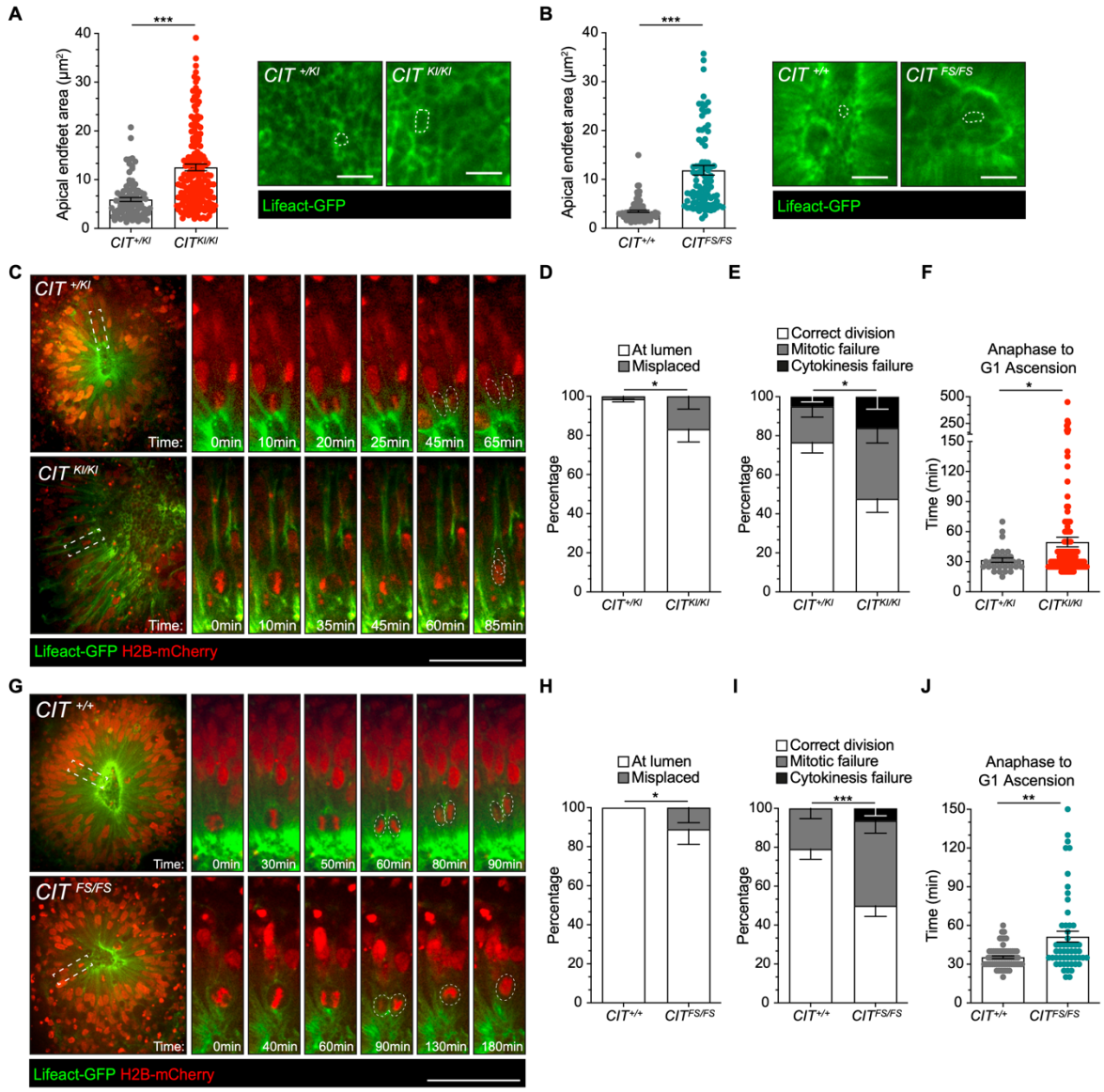

(**A-B**) Apical endfeet area and a representative image of 35DD organoid apical surface labeled with Lifeact-GFP in microfabricated compartments. Apical endfeet surface area is increased in affected *CIT*$^{KI/KI}$ (A) and *CIT*$^{FS/FS}$ (B) compared to *CIT*$^{+/KI}$ *and CIT*$^{+/+}$ control organoids. Scale bars =10µm

(**C**) Representative images from videos of *CIT*$^{+/KI}$ and *CIT*$^{KI/KI}$ rosettes with aNPC mitotic division (white rectangle) at the apical surface. Panel demonstrates time details of this division. Scale bar = 50µm

(**D**) Quantification of the percentage of division occurring at central lumen or misplaced from the lumen of (C).

(**E**) Quantification of the percentage of correct division, mitotic failure, and cytokinesis failure of (C).

(**F**) Measurement of time spent from anaphase to G1 ascension in $CIT^{+/KI}$ and $CIT^{KI/KI}$ aNPC divisions in 35DD organoid rosettes. Each dot indicates a single dividing cell.

(**G**) Representative images from videos of $CIT^{+/+}$ and $CIT^{FS/FS}$ rosettes with aNPC mitotic division (white rectangle) at the apical surface. Panel demonstrates time details of this division. Scale bar = 50μm

(**H**) Quantification of the percentage of division occurring at central lumen or misplaced from the lumen of (G).

(**I**) Quantification of the percentage of correct division, mitotic failure, and cytokinesis failure of (G).

(**J**) Measurement of time spent from anaphase to G1 ascension in $CIT^{+/+}$ and $CIT^{FS/FS}$ aNPC divisions in 35DD organoid rosettes. Each dot indicates a single dividing cell. Quantification from a minimum of two independent compartment preparations per genotype. Compartments each contain ≤ 9 organoids per preparation. Error bars, SEM. *P<0.05, **P<0.01, ***P<0.001; Unpaired two-tailed Student's t-test for apical endfeet area, Fisher Exact Probability Test for percentage distribution, Mann–Whitney U test for time from anaphase to G1 ascension.

<u>Figure 6</u> *CIT* affected organoids show accumulation of DNA damage and apoptosis

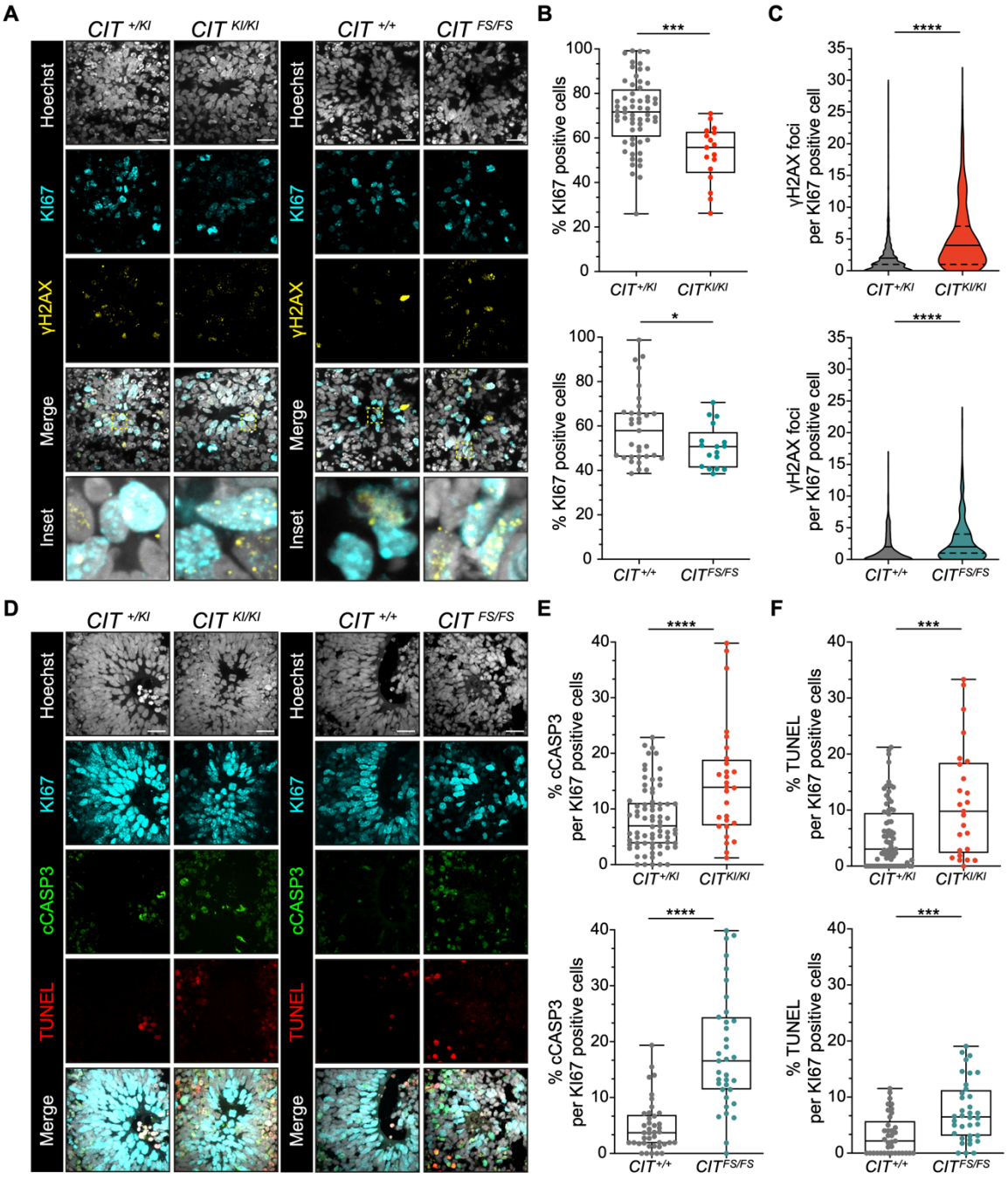

(**A**) Representative images of rosettes for indicated *CIT* genotypes for DNA damage marker γH2AX (yellow), proliferation marker KI67 (cyan) and Hoechst (gray). Scale bars = 20µm

(**B-C**) Quantification of KI67-positive cells (B) and of γH2AX foci per KI67-positive nucleus (C). >500 cells were counted for each genotype in each replicate.
(**D**) Representative images of rosettes for indicated *CIT* genotypes for apoptotic marker cCASP3 (green), TUNEL assay (red), proliferation marker KI67 (cyan) and Hoechst (gray). Scale bars = 20μm
(**E-F**) Quantification of cCASP3 (E) and TUNEL (F) staining per KI67-positive cells. Every dot represents a neural rosette. Quantification from a minimum of 3 independent organoid preparations. Error bars, SEM. *P<0.05, ***P<0.001, ****P<0.0001; unpaired two-tailed Student's t-test. Mann–Whitney U test was used for γH2AX foci.